RSC Advances

PAPER

View Article Online
View Journal | View Issue

Cite this: *RSC Adv.*, 2023, **13**, 28389

Facile synthesis of sulfide $Bi_{13}S_{18}I_2$ as a promising anode material for a lithium-ion battery†

Cheng-Lu Yang,[a] Chen Liang,[a] Chao Gao,[ab] Jun Guo, *[ab] Bu-Ming Chen *[abc] and Hui Huang[abc]

Received 19th July 2023
Accepted 10th September 2023

DOI: 10.1039/d3ra04845d

rsc.li/rsc-advances

A novel $Bi_{13}S_{18}I_2$ structure was synthesized using a facile one-pot hydrothermal method and further optimized as an anode material using graphene. The graphene/$Bi_{13}S_{18}I_2$ composite achieved a high discharge capacity with an initial value of 1126.5 mA h g^{-1} and a high and stable discharge capacity of 287.1 mA h g^{-1} after 500 cycles compared with pure $Bi_{13}S_{18}I_2$, which derives from the inhibited volume expansion and high electrical conductivity obtained from graphene. *In situ* XRD was performed to analyze the Li storage mechanism in depth. The results support the feasibility of the new ternary sulfide $Bi_{13}S_{18}I_2$ as a promising lithium ion battery.

1. Introduction

With the development of the global new-energy industry, its main power storage, the lithium battery, has become a concentrated field of energy industry growth and has been widely used in mobile communication, computing, electric vehicles, aerospace, and other fields, becoming one of the key products of high-tech development. Lithium-ion batteries (LIBs) have the advantages of high energy density, long cycling life, small self-discharge, and wide operating temperature range, among others.[1–3] Conventional commercial graphite anodes have low theoretical capacitance (372.0 mA h g^{-1}) and poor rate capacity, which are far from meeting the high energy/power density of LIBs.[4–7] To improve the performance of LIBs, various active materials have been investigated. Carbon-based materials, alloys and transition metal sulfides have been investigated owing to their theoretical capacity.[8–13]

Metal sulfides, having low cost, high theoretical capacity and suitable working voltage, have been regarded as promising anode materials. The theoretical capacity of the transition metal sulfides M_xS_y (M = Fe, Ni, Co and Cu) is nearly two times higher than that of the commercial graphite electrode; they avoid the formation of lithium dendrites and ensure high safety. They have gained wide attention due to the transition metal sulfide layered structure, super high specific capacity, and relatively stable performance.[14–18] Among the transition metal sulfides, bismuth sulfide-based anode materials have been noticed, due to their relatively high electrical conductivity and theoretical capacity. Bi_2S_3 is a classical bismuth sulfide-based anode material that has received much attention due to its higher theoretical capacity of 625.0 mA h g^{-1};[19,20] besides, Bi_2S_3 is earth abundant, low cost, and environmentally friendly. However, as an anode material, Bi_2S_3 suffers from large volume changes during the charging and discharging process, unstable formation of solid electrolyte interface (SEI) film, and inherently poor electrical conductivity.[2] Excessive volume expansion leads to particle comminution, fast capacity attenuation, and unsatisfactory electrochemical performance.

Strategies have been used to overcome the shortcomings of the Bi_2S_3 anode, and a typical method to improve the electrochemical stability of anodes is the combination of the anode and carbon material, including carbon composites (core–shell Bi_2S_3@C,[21] Bi_2S_3@Py[22,23]) and carbon coating technology (Bi_2S_3/C[8,12,21] nanorods, Bi_2S_3-CNT[19]). It is desirable to explore inorganic/organic ternary mixed anionic compounds such as bismuth-based materials as components of battery electrodes. Among the ternary mixed anionic materials, $Bi_{13}S_{18}I_2$ is a classical ternary bismuth sulfide material. $Bi_{13}S_{18}I_2$ has a different symmetry in its crystal structure, along with the introduction of some new structural motifs, resulting in substantial modification of the electronic and harmonic structure. Binary Bi_2S_3 anode material shows good discharge capacity and stability when encapsulated with carbon through carbonization by conducting polymer at high temperature.[22] Ternary $B_{13}S_{18}I_2$ possesses a special crystal structure that gives it better electrical conductivity than Bi_2S_3. Therefore, $B_{13}S_{18}I_2$ has potential as a promising anode using a suitable optimization method. However, the thermal stability of $B_{13}S_{18}I_2$ is poor, so its capacity stability is optimized by compositing with direct carbon materials.[24] Graphene was confirmed to be a good anode additive[25]

[a]*Faculty of Metallurgical and Energy Engineering, Kunming University of Science and Technology, Kunming, 650093, China. E-mail: 1038gj@kust.edu.cn; bumchen@kust.edu.cn*

[b]*Research Center of Yunnan Metallurgical Electrode Materials Engineering Technology, Kunming 650106, China*

[c]*Kunming Hendera Science and Technology Co., Ltd, Kunming 650106, China*

† Electronic supplementary information (ESI) available. See DOI: https://doi.org/10.1039/d3ra04845d

that is beneficial for improving the electrical conductivity and discharge stability of anode materials. Graphene sheet (GS) can effectively inhibit the aggregation of components and further improve the electrical conductivity due to its unique three-dimensional porous structure,[23] which results in accelerated transport between Li^+ and electrons, greatly improving the electrochemical performance.[24,25]

N-doping not only improves the electrical conductivity of graphene but also incorporates more defects, which promotes more active sites for Li storage. N element was doped into graphene using a hydrothermal process and adding urea. The improved electrical conductivity promotes the charge transfer kinetics during discharging/charging and maintains structural stability during the cycling process. Similar introduction of N sources has been reported, *e.g.*, (a) GaN@NG heterojunction;[26] (b) N-doped hollow urchin-like anatase TiO_2@C; (d) Cu_6Sn_5/Cu composite;[27] and (e) biomass-derived nanostructured carbons.

In this work, a new bismuth sulfide, $Bi_{13}S_{18}I_2$, was synthesized by a facile hydrothermal method, and graphene was used to optimize the electrical conductivity and cycle stability of $Bi_{13}S_{18}I_2$. The results show that the composites exhibit excellent electrochemical performance as anode materials for Li-ion batteries, with an initial discharge capacity of 1126.5 mA h g^{-1} and a specific discharge capacity of 287.0 mA h g^{-1} after 500 cycles. The improved electrochemical performance is attributed to the introduction of graphene oxide flakes, which not only buffer the large volume changes of Li and Bi during the lithiation/desulfuration process but also enhance the electrical conductivity. The N-doping in graphene further improves the sample electrical conductivity and activation site for Li storage. It has great potential for practical applications in high-performance lithium-ion batteries.

2. Experimental section

Synthesis of materials: bismuth nitrate pentahydrate ($Bi(NO_3)_3 \cdot 5H_2O$, 99.9%), thiourea (CN_2H_4S, 99.99%), sodium iodide (NaI, 99.99%), and graphene (C, 98%) were purchased from Aladdin and used as starting materials without further purification. BSI composites with different graphene contents were designated as 100 G/BSI, 150 G/BSI, and 200 G/BSI. Detailed information regarding the experimental procedures is provided in the ESI (ESI†).

3. Results and discussion

FE-SEM was performed to observe the microstructure of the synthesized graphene/BSI samples, and the result is shown in Fig. 1a. Both morphologies of flaky graphene and spherical BSI can be clearly observed. The microscale is well fixed on the graphene flakes; the graphene layer thickness is uniform, and no obvious aggregation of graphene and BSI particles was observed in the image. The special morphology not only significantly promotes charge transport and ion migration, but also effectively alleviates the volume expansion during cycling, which is conducive to improving electrochemical activity and prolonging cycle life. As shown in Fig. 1b, it is observed in EDS

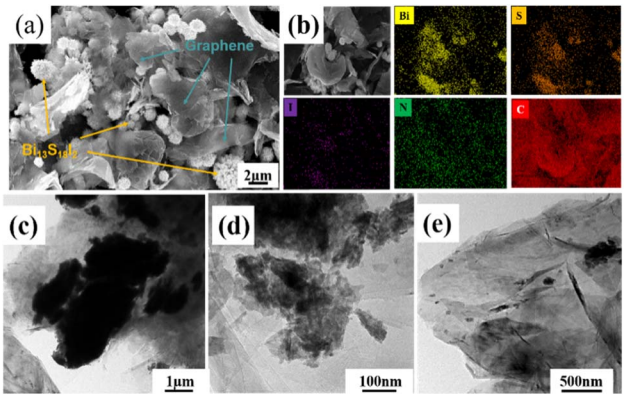

Fig. 1 (a) 150 G/BSI FE-SEM; (b) EDS mapping and (c–e) HRTEM images of the 150 G/BSI.

mapping that the flakes are graphene with mainly carbon and nitrogen enrichment. The elements Bi, S and I are uniformly distributed on the urchin-like samples, and the results are in agreement with XRD. This indicates that graphene is successfully doped with N element, and Fig. S1† further confirms the uniform distribution of BSI in graphene. As shown in Fig. S2,† the sample before cycling consists of urchin-shaped BSI and flake-like graphene, and the sample before cycling is uniformly distributed with better crystallinity and clearer powder contour. During cycling, the volume of the powder undergoes repeated expansion and shrink, which eventually leads to the collapse of the BSI sample structure after cycling; the powder starts to break up. Graphene is seriously agglomerated, which leads to the degradation of sample performance and poor cycling performance. HRTEM images further confirm that the microscale BSI particles were well wrapped by the carbon film (Fig. 1c–e), and the carbon layer could also provide a larger buffer space and better buffering effect.

X-ray diffraction (XRD) patterns of all BSI samples with graphene addition are shown in Fig. 2a. All diffraction peaks of the graphene/BSI composites and the pure BSI match well with the BSI orthorhombic crystals according to the standard PDF card no. 73-1157, and the diffraction peaks of (130), (121), (301) and (221) facets of BSI are obvious, indicating that the products have high crystallinity. A peak of (111) crystal plane near 25.8° is observed in the XRD pattern after graphene addition, confirming the introduction of crystalline graphene. The synthesized graphene/BSI composites' XRD spectra are similar to pure BSI, indicating that the introduction of graphene has no obvious effect on the microscale BSI. The Raman spectrum of 150 G/BSI is shown in Fig. S3.† The Raman spectrum shows two typical broad bands of graphene/BSI composites with distinct D (sp^{-3} hybridized disordered) and G (sp^{-2} hybridized) bands of carbon material at 1350 cm and 1580 cm, respectively.[22] The G band corresponds to the stretching mode of the CvC bond of graphite, while the D band is attributed to the vibrations of carbon atoms with dangling bonds at the planar ends of disordered graphite, which confirms the crystalline carbon structure. The results further suggest that the BSI nanospheres are covered with a carbon layer on the surface. Furthermore, the

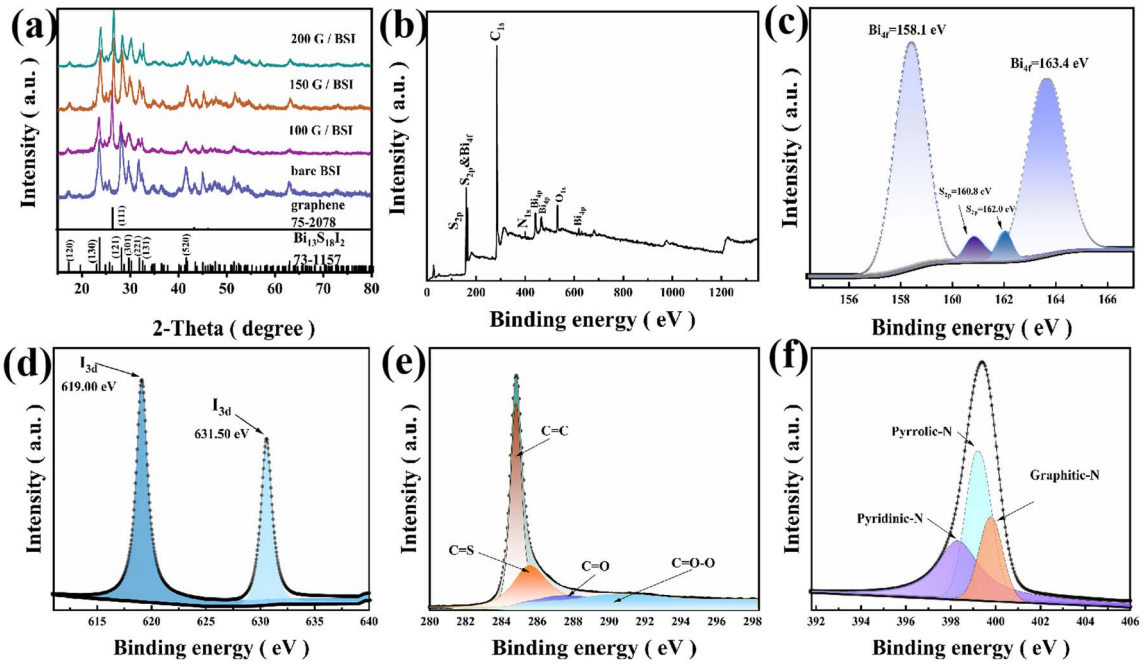

Fig. 2 (a) XRD patterns of 100 G/BSI, 150 G/BSI, 200 G/BSI and bare BSI composites; (b) the XPS survey spectrum, and corresponding high-resolution XPS spectra of (c) S and Bi, (d) I, (e) C, and (f) N for the 150 G/BSI composite spheres.

calculated I_D/I_G of 1.0 from the image indicates the presence of a large number of defects in the crystalline carbon, probably due to N doping effects. The peak intensity ratio (I_D/I_G) in the D and G bands reflects the degree of graphitization of the composite. The higher intensity of the G-band in 150 G/BSI indicates that there is more graphitic carbon in the material. The chemical composition and valence states of the samples were investigated by X-ray photoelectron spectroscopy (XPS). Fig. 2b shows the XPS survey spectrum of the 150 G/BSI sample, indicating the presence of Bi, S, I, N and C in the graphene/BSI sample, which is in good agreement with the above EDS mapping results. Fig. 2c shows the high-resolution spectra of S 2p and Bi 4f, with two distinct peaks located at 158.1 and 163.4 eV corresponding to Bi $4f_{7/2}$ and Bi $4f_{5/2}$, respectively, while two distinct peaks located at 160.8 and 162.0 eV correspond to S $2p_{3/2}$ and S $2p_{1/2}$, respectively,[17] which indicate the existence of S^{2-} and Bi^{3+}. For the high-resolution I 3d spectra, two intense characteristic peaks were observed at 619.0 eV and 631.50 eV, indicating the presence of I^- (Fig. 2d). Additionally, there were four different peaks at 284.8, 286.0, 287.9 and 291.3 eV observed, which can be interpreted as C–C, C–S, C–O and C═O–O, respectively.[22] For the high-resolution N 1s spectra (Fig. 2e), the peaks at 398.6, 399.7 and 400.2 eV can be attributed to pyridine N, pyridine N and graphite N doped in the carbon matrix,[28] respectively, further indicating that the N atoms were successfully doped into the carbon during the annealing process. The doped N in the carbon matrix can greatly improve its electrical conductivity and surface hydrophilicity, thus enabling fast charge transfer and ion diffusion.[23] Furthermore, pyridine N provides additional active sites for lithium-ion storage, further increasing the capacity.[24]

The electrochemical performance of the graphene/BSI samples was evaluated using cyclic voltammogram (CV) and galvanostatic tests to investigate their feasibility as potential anode materials for LIBs. Fig. 3a shows the CV curves of the 150 G/BSI sample for the first three cycles with the scan rate of 0.2 mV s^{-1} and the voltage range of 0.01–3 V (*vs.* Li^+/Li). During the first cathodic scan, peaks at 1.6 V are attributed to the conversion of BSI to metal Bi, and a minor peak appearing at 0.69 V could be ascribed to the formation of LiBi alloy, which is known to form at 0.61 V.[8,29] The anodic peak of the conversion reaction is weaker than the cathodic peak, indicating that part of the BSI cannot be recovered, leading to irreversible capacity loss. During the first cathodic process, a small irreversible reduction peak appeared at about 0.25 V, which may be related to the reduction of the remaining oxygen in graphene.[30] The position and intensity of the peak remained almost unchanged in the subsequent cycles, suggesting that graphene/BSI has good reversibility for lithium storage. The charge/discharge curves for 150 G/BSI are shown in Fig. 3b. It can be clearly seen that the first charge capacity is 401.2 mA h g^{-1}; the tenth cycle discharge capacity is 500.6 mA h g^{-1}. The homogeneity of graphene favors the formation of a stable SEI layer and generates more lithium storage sites. The irreversible capacity loss of 19.8% is attributed to the formation of SEI layer on the surface of the active material and the partial deactivation products due to the conversion and alloying reactions. Prior to the alloying reaction, Li^+ reduces $Bi_{13}S_{18}I_2$ to Bi and Li_2S, resulting in a large electrode polarization and voltage lag between the lithiation and oxidation reactions.

Surface remodeling of the $Bi_{13}S_{18}I_2$ and SEI layers may occur during cycling, and at the 30th and 50th cycles, the charge and

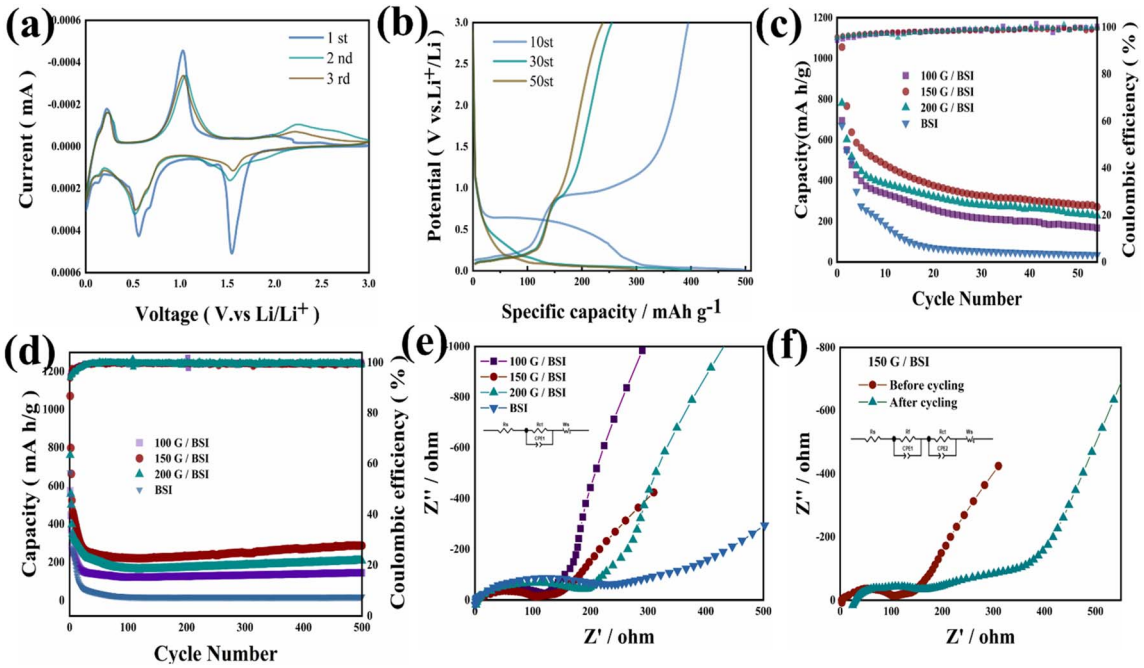

Fig. 3 (a) CV curves of BSI at a sweep rate of 0.2 mV s^{-1} for the first three cycles; (b) charge–discharge curves of 150 G/BSI at 10, 30 and 50 cycles; (c) cycle stability at the current density of 0.05 A g^{-1}; (d) long cycling performance at 0.5 A g^{-1}; (e) impedance spectra before cycles; (f) impedance spectra after cycles.

discharge curves overlap well and show good structural stability. The charge/discharge capacities of the 150 G/BSI electrode are 402.5 mA h g^{-1} and 398.6 mA h g^{-1}, respectively. Finally, the reversible charging capacities are maintained at 251.0 mA h g^{-1} and 248.7 mA h g^{-1}. During the discharging process, plateaus were observed in the range of 0.5–0.7 V. Combined with the 10th discharge curve and Fig. S7,† the observed plateau in the 10th cycle at about 0.5–0.7 V could stem from the formation of Li–Bi alloy. Meanwhile, during the charging process, peaks were observed at 0–0.5 V and 0.75–1.0 V, which is consistent with the CV analysis results. The cycling performance of pure BSI and all the graphene-added BSI samples was tested under the current density of 0.05 A g^{-1} in the range of 0.01–3.0 V. As shown in Fig. 3c, the initial discharge capacities of pure BSI, 100 G/BSI and 200 G/BSI are 670.0, 695.0 and 781.4 mA h g^{-1}, respectively, which is much lower than the 1126.5 mA h g^{-1} for 150 G/BSI. This indicates that the addition of graphene has a positive effect on improving the capacity of BSI, and 150 mg is the optimal amount of graphene addition. The capacity of pure BSI rapidly decays in the subsequent cycles due to the large volume expansion behavior during the charge and discharge process. The results for 500 cycles are shown in Fig. 3d. Although 100 G/BSI suffers from capacity loss in the first few cycles, it still maintains a discharge capacity of about 200 mA h g^{-1} after 500 cycles. The discharge capacity of the 150 G/BSI sample decreases from 1126.5 to 287.1 mA h g^{-1} after 500 cycles, which may be ascribed to the destruction of sample structure during the charge–discharge process. As seen in Fig. S2,† the samples possessed good crystalline and clear morphology before cycling. However, after cycling, graphene was agglomerated and the surface structure of $B_{13}S_{18}I_2$ was broken during the charge–discharge process, leading to the rapid decline in capacity. After extended cycling, the SEI protective layer formed, giving rise to the stable capacity of 287.1 mA h g^{-1}. The capacity increase after prolonged cycling was attributed to the co-activation phenomenon of the oxide and sulfide anodes, indicating SEI stability.[18] Furthermore, the discharge capacity of bare graphene as the anode was explored. As shown in Fig. S4,† a low discharge capacity of 133 mA h g^{-1} was observed for bare graphene after 500 cycles at the current density of 0.5 A g^{-1}. Combined with the limited addition of graphene, the result shows that graphene contributes limited capacity to the BSI system.

Furthermore, the coulombic efficiency of all BSI samples was maintained above 98% after 500 cycles. The higher cycling stability of graphene/BSI compared with pure BSI originates from the introduced graphene, which acts as a protective layer to buffer the volume expansion of the cell during charging and discharging. The 150 G/BSI electrode has a high initial discharge capacity and excellent stability, mainly attributed to the fact that graphene was moderately coated on BSI to inhibit the variation of volume. N doping improves the electrical conductivity of all samples and provides a large number of active sites for lithium storage in the carbon layer. The rate performance images of pure BSI and 150 G/BSI are shown in Fig. S5;† the current density values were set to 0.05, 0.1, 0.2, 0.5 and 0.8 A g^{-1} and returned to 0.1 A g^{-1} for the last 20 cycles; the capacity of the 150 G/BSI electrode was maintained at 256.6 mA h g^{-1}, indicating a good capacity recovery. In contrast, the pure BSI electrode could only maintain 161.5 mA h g^{-1}. The high rate performance of the 150 G/BSI was due to the graphene coating and nitrogen doping.

Graphene plays a very important role in improving the electrochemical properties of graphene/BSI composites. To reveal the origin of improved electrochemical performance in the graphene/BSI electrodes, electrochemical impedance spectroscopy (EIS) was performed, and the data were fitted by Z-View software using an equivalent circuit model, where R_e is the test cell internal resistance, R_{ct} and CPE are related to the charge transfer resistance at the electrode/electrolyte interface and constant phase, Z_W is related to the Warburg impedance corresponding to the lithium ion diffusion process, the semicircle in the high-frequency region of the EIS plot is related to the formation of the SEI film (R_{SEI}), the decreasing semicircle in the medium frequency is attributed to the charge transfer reaction at the electrode/electrolyte interface (R_{ct}), and the low-frequency straight line reflects the diffusion of lithium ions in the electrode material.[24–26] Fig. 3e shows the electrochemical impedance curves of pure BSI and all graphene/BSI samples before cycling; the curves are characterized by a semicircle in the high-frequency region and linear slope in the low-frequency region of the impedance plot, which correspond to R_{ct} and the Li^+ ion diffusion process, respectively. It can be clearly seen that the semicircle diameter of the 150 G/BSI is smaller than that of the other electrodes before cycling, indicating that the resistance to interfacial charge transfer is smaller and the conductivity is better. The impedance of the sample was elevated again after the graphene addition amount reached 200 mg, which was mainly because graphene was prone to agglomeration, thus impeding electron transport and, instead, leading to the decrease of electrical conductivity. The fitted impedance parameters are shown in Table S1.† It can be seen that the R_e and R_{ct} of the 150 G/BSI composite electrode are 6.85 Ω and 104.6 Ω, which are lower than those of the other two composite electrodes, and the results confirm that the addition of 150 mg graphene not only maintains the high electrical conductivity of the BSI/graphene composite electrode but also greatly enhances the fast electron transfer in the electrochemical insertion of the lithium extraction process, which can significantly improve the BSI/graphene composites' electrochemical performance. The post-cycling EIS data in Fig. 3f shows the formation of the second semicircle, which originates from the formation of SEI film on the surface of the cycled sample, leading to the increased interface resistance.[31] The results confirm that N-doped graphene not only maintains the high conductivity of the BSI composites, but also greatly improves the fast electron transfer during electrochemical lithium insertion/extraction and effectively suppresses the volume expansion during charge/discharge, thus significantly improving the electrochemical performance of the graphene/BSI composite. Meanwhile, diffusion kinetics of lithium ions in electrodes can be obtained according to the Warburg factor (r) related to the slope of the linear fittings in the low-frequency region. The $Z' - x^{-1/2}$ (x = 2pf) curve region and diffusion coefficient (D_{Na}, $cm^2\ s^{-1}$) can be calculated according to the following equations:

$$Z = R_e + R_{ct} + \sigma\omega^{-1/2}$$

$$D = R^2T^2/2A^2n^4F^4C^2\sigma^2$$

In the equations, A is electrode area, F is Faraday's constant, x is the angular frequency, R is gas constant, C is molar concentration of LI^+, T is testing temperature, n is the reactive electron number per molecule, and r is the Warburg factor. According to Fig. S6,† the calculated D_{Na} values for the 100 G/BSI, 150 G/BSI, and 200 G/BSI electrodes are 9.8×10^{-13} $cm^2\ s^{-1}$, 8.517×10^{-13} $cm^2\ s^{-1}$, and 1.04×10^{-12} $cm^2\ s^{-1}$. It is shown that the 150 G/BSI electrode has faster ion diffusion kinetics.

Furthermore, *in situ* XRD was performed to investigate the Li-storage mechanism of graphene/BSI (Fig. S7†). During the initial lithiation, the diffraction peak of BSI gradually decays, while the characteristic peaks of intermediate LiBi appear at 2-theta = 25.8° and 35.1°. After further alloying, these characteristic peaks are assigned to the intermediate product of the lithiation process, Li_3Bi, with the peak appearing at 2-theta = 27.3°, probably due to the *in situ* measurements avoiding the hydrolysis of the sample during the post-treatment. At the end of the discharge process, only the Li_3Bi peak was detected in the XRD pattern, indicating the complete conversion of BSI and LiBi to the final phase Li_3Bi. During the charging process, the diffraction peak of Li_3Bi appeared, followed by the reappearance of the LiBi phase. In addition, the characteristic peak of BSI can be clearly observed in the fully charged state at 2.8 V. The BSI conversion fraction produces LiBi, followed immediately by Li_3Bi to complete the dehydrogenation from LiBi to Bi. The XRD spectrum of charged $Bi_{13}S_{18}I_2$ matches that of metal Bi after alloy treatment, and the evolution of the pattern confirms the good reversibility of the phase change during the cycling process.[32–34] The relevant phase variation during the charge/discharge procedure is shown in ESI.†

4. Conclusions

In summary, a novel $Bi_{13}S_{18}I_2$ was synthesized by a facile hydrothermal method, and the electrical conductivity and cyclic stability of $Bi_{13}S_{18}I_2$ were optimized by using N-doped graphene. The graphene-coated urchin-like $Bi_{13}S_{18}I_2$ structure prevents the aggregation of powders during the synthesis process and greatly improves the cycling stability and rate capability of the cell compared with pure BSI. The improved cycling stability mainly originates from the introduced graphene sheets, which inhibit the volume expansion of microscale BSI during the charging and discharging procedure. The improved rate capability originates from the high electrical conductivity of graphene sheets, which greatly enhances the transfer of electrons during the electrochemical reaction of the graphene/BSI composite electrode. The lithium ion storage mechanism of graphene/BSI composites was further investigated by *in situ* XRD measurements. The results indicate that the new graphene/BSI composites have great potential for applications in lithium-ion batteries.

Author contributions

Cheng-Lu Yang: investigation, writing – original draft, conceptualization. Chen Liang: investigation. Chao Gao: investigation.

Jun Guo: conceptualization, methodology, writing – original draft. Bu-Ming Chen: methodology. Hui Huang: conceptualization, methodology.

Conflicts of interest

There are no conflicts to declare.

Acknowledgements

This work was supported by the National Natural Science Foundation of China (grant no. 52274409) and Yunnan province technical innovation talent project (grant no. 2019HB111).

Notes and references

1 X. Chen, P. Wang, Z. Zhang and L. Yin, *J. Alloys Compd.*, 2020, **844**, 156008.
2 R.-M. Gao, Z.-J. Zheng, P.-F. Wang, C.-Y. Wang, H. Ye and F.-F. Cao, *Energy Storage Mater.*, 2020, **30**, 9–26.
3 L. Silvestri, M. A. Navarra, S. Brutti and P. Reale, *Electrochim. Acta*, 2017, **253**, 218–226.
4 L. Jiang, Z. Zhang, F. Liang, D. Wu, K. Wang, B. Tang, Y. Rui and F. Liu, *Dalton Trans.*, 2021, **50**, 9775–9786.
5 M. N. Obrovac and V. L. Chevrier, *Chem. Rev.*, 2014, **114**, 11444–11502.
6 Q. Pan, Q. Zhang, F. Zheng, Y. Liu, Y. Li, X. Ou, X. Xiong, C. Yang and M. Liu, *ACS Nano*, 2018, **12**, 12578–12586.
7 Z. Zheng, Y. Zao, Q. Zhang, Y. Cheng, H. Chen, K. Zhang, M.-S. Wang and D.-L. Peng, *Biochem. Eng. J.*, 2018, **347**, 563–573.
8 W. Chai, F. Yang, W. Yin, S. You, K. Wang, W. Ye, Y. Rui and B. Tang, *Dalton Trans.*, 2019, **48**, 1906–1914.
9 L. Zhao, H. H. Wu, C. Yang, Q. Zhang, G. Zhong, Z. Zheng, H. Chen, J. Wang, K. He, B. Wang, T. Zhu, X. C. Zeng, M. Liu and M. S. Wang, *ACS Nano*, 2018, **12**, 12597–12611.
10 Y. Yu, L. Gu, C. Zhu, S. Tsukimoto, P. A. van Aken and J. Maier, *Adv. Mater.*, 2010, **22**, 2247.
11 Q. Pan, F. Zheng, Y. Liu, Y. Li, W. Zhong, G. Chen, J. Hu, C. Yang and M. Liu, *J. Mater. Chem. A*, 2019, **7**, 20229–20238.
12 M. K. Kim, M. S. Kim, J. H. Park, J. Kim, C. Y. Ahn, A. Jin, J. Mun and Y. E. Sung, *Nanoscale*, 2020, **12**, 15214–15221.
13 H. Dong, M. Deng, D. Sun, Y. Zhao, H. Liu, M. Xie, W. Dong and F. Huang, *ACS Appl. Energy Mater.*, 2022, **5**, 3463–3470.
14 P. Poizot, S. Laruelle, S. Grugeon, L. Dupont and J. M. Tarascon, *Ionics*, 2000, **6**, 321–330.
15 Q. Pan, F. Zheng, Y. Wu, X. Ou, C. Yang, X. Xiong and M. Liu, *J. Mater. Chem. A*, 2018, **6**, 592–598.
16 Y. Huang, X. Hu, J. Li, J. Zhang, D. Cai, B. Sa, H. Zhan and Z. Wen, *Energy Storage Mater.*, 2020, **29**, 121–130.
17 W. Zhang, J. Wu, Y. Li, X. Feng, L. Wang, X. He, N. L. Wu, M. Ouyang and M. Wei, *J. Colloid Interface Sci.*, 2022, **625**, 692–699.
18 Y. Dong, M. Hu, Z. Zhang, J. A. Zapien, X. Wang and J. M. Lee, *Nanoscale*, 2018, **10**, 13343–13350.
19 W. Yang, H. Wang, T. Liu and L. Gao, *Mater. Lett.*, 2016, **167**, 102–105.
20 J. Sottmann, M. Herrmann, P. Vajeeston, A. Ruud, C. Drathen, H. Emerich, D. S. Wragg and H. Fjellvåg, *Chem. Mater.*, 2017, **29**, 2803–2810.
21 Z. Liu, S. Jin, K. Cui, J. Zhao, S. Xie, J. Li and C. Xinghua, *J. Alloys Compd.*, 2020, **842**, 155796.
22 H. Liang, J. Ni and L. Li, *Nano Energy*, 2017, **33**, 213–220.
23 B. Long, Z. Qiao, J. Zhang, S. Zhang, M.-S. Balogun, J. Lu, S. Song and Y. Tong, *J. Mater. Chem. A*, 2019, **7**, 11370–11378.
24 Z. Zhang, C. Zhou, L. Huang, X. Wang, Y. Qu, Y. Lai and J. Li, *Electrochim. Acta*, 2013, **114**, 88–94.
25 S. Wang, R. Wang, Q. Zhao, L. Ren, J. Wen, J. Chang, X. Fang, N. Hu and C. Xu, *J. Colloid Interface Sci.*, 2019, **544**, 37–45.
26 C. Sun, Y.-J. Wang, D. Liu, B. Fang, W. Yan and J. Zhang, *Chem. Eng. J.*, 2023, **453**, 139603.
27 Y. Xing, S. Wang, B. Fang, Y. Feng and S. Zhang, *Microporous Mesoporous Mater.*, 2018, **261**, 237–243.
28 Y. Huang, X. Zhu, D. Cai, Z. Cui, Q. Wang and H. Zhan, *J. Energy Chem.*, 2021, **59**, 473–481.
29 H. Yue, S. Chen, P. Li, C. Zhu, X. Yang, T. Li and Y. Gao, *Ionics*, 2019, **25**, 3587–3592.
30 P. Kumar, W. Wahyudi, A. Sharma, Y. Yuan, G. T. Harrison, M. Gedda, X. Wei, A. El-Labban, S. Ahmad, V. Kumar, V. Tung and T. D. Anthopoulos, *Chem. Commun.*, 2022, **58**, 3354–3357.
31 C. Liang, P. Zhang, H. Huang, C. Gao, J. Guo and Y. He, *Ionics*, 2023, **29**, 2573–2586.
32 Y. Zhang, X. Yuan, T. Lu, Z. Gong, L. Pan and S. Guo, *J. Colloid Interface Sci.*, 2021, **585**, 347–354.
33 N. Cao, L. Wen, Z. Song, W. Meng and X. Qin, *Electrochim. Acta*, 2016, **209**, 235–243.
34 X. Li, J. Liang, Z. Hou, W. Zhang, Y. Wang, Y. Zhu and Y. Qian, *Adv. Funct. Mater.*, 2015, **25**, 5229–5238.